

# INVESTIGATION OF A HIGH-PRESSURE TURBINE STAGE IN A HIGH-SPEED ROTATING TRANSIENT TEST FACILITY FOR ROTOR TIP STUDY AND A PARAMETRIC STUDY FOR IMPROVED HEAT TRANSFER CALCULATION

**Deepanshu Singh**  
Oxford Thermofluids  
Institute,  
Department of Engineering  
Science  
University of Oxford  
OX2 0ES, UK  
[deepanshu.singh@eng.ox.ac.uk](mailto:deepanshu.singh@eng.ox.ac.uk)

**Paul F. Beard**  
Oxford Thermofluids  
Institute,  
Department of  
Engineering Science  
University of Oxford  
OX2 0ES, UK  
[paul.beard@eng.ox.ac.uk](mailto:paul.beard@eng.ox.ac.uk)

**David Cardwell**  
Oxford Thermofluids  
Institute,  
Department of  
Engineering Science  
University of Oxford  
OX2 0ES, UK  
[david.cardwell@eng.ox.ac.uk](mailto:david.cardwell@eng.ox.ac.uk)

**Kam S. Chana**  
Oxford Thermofluids  
Institute,  
Department of  
Engineering Science  
University of Oxford  
OX2 0ES, UK  
[kam.chana@eng.ox.ac.uk](mailto:kam.chana@eng.ox.ac.uk)

## ABSTRACT

*The first part of the paper presents commissioning of a single-stage high-pressure turbine employed in a series of extensive experiments to study the aerodynamics and heat transfer on the rotor surface and casing liner. The OTRF (Oxford Turbine Research Facility), a high-speed rotating transient test facility has the capability to take unsteady aerodynamic and heat transfer measurements at engine representative conditions with a variety of inlet temperature profiles including radial distortion and swirl. A temperature profile survey was conducted at the inlet of the high-pressure NGV (Nozzle Guide Vane). Static and total pressure and temperature measurements have been taken at various locations on the rig including NGV surface, inlet and exit, and rotor exit to establish rig operating conditions. Detailed description of mass flow rate measurements along with calculation of heat loss factor in the rig is presented. The second part of the paper presents a parametric study performed to improve heat transfer measurement calculations from high-frequency response thin-film gauges. The effect of parameters like material properties and thickness of substrate on heat flux has been studied. A detailed uncertainty analysis for heat flux is also presented. A thermal model calibrated with analytical solutions has been developed to optimise thin-film gauge configurations and to study side-conduction effects.*

## NOMENCLATURE

$\alpha_{cal}$	Temperature coefficient of resistance
$\alpha$	Thermal diffusivity
$t$	Time
$f_s$	Sampling frequency
$np$	Total number of samples
$R$	Resistance of thin-film gauge/gas constant
$R_o$	Initial resistance of thin-film gauge
$m$	Mass flow rate
$A_{geo}$	Geometric area of the throat
$A_{eff}$	Effective area of the throat
$M$	Mach number

$P$	Pressure
$T$	Temperature
$\gamma$	Ratio of specific heat
$C_p$	Specific heat capacity
$T_{o,eff}$	Total temperature effectiveness
$\theta$	Heat loss factor
$Re$	Reynolds number
$Nu$	Nusselt number
$Pr$	Prandtl number
$I_e$	Gauge excitation current
$\rho_r$	Electrical resistivity
$\rho$	Density
$V$	Voltage of thin-film gauge
$w$	Width of thin-film gauge
$l$	Length of thin-film gauge
$a$	Thickness of thin-film gauge
$\dot{q}$	Heat flux
$k$	Thermal conductivity
$x^*$	Non-dimensional penetration depth
$\sigma_i$	Uncertainty in variable 'i'

## Subscripts

$0$	Stagnation conditions
$1$	NGV inlet
$2$	Rotor inlet
$c$	RTDF cold stream
$h$	Hot stream
$h_{corr}$	Corrected hot stream
$w$	Wall
$c_{NGV}$	NGV cold flow
$s$	Surface value

## Abbreviations

OTRF	Oxford Turbine Research Facility
RTDF	Radial Temperature Distortion Factor
NGV	Nozzle Guide Vane

SILOET	Strategic Investment in Low-Carbon Engine Technology
NGV	Nozzle Guide Vane
FFT	Fast Fourier Transform
erfc	Complimentary error function
exp	Exponential function
RPM	Rotations per minute
htc	Heat transfer coefficient
HP	High Pressure

## 1. INTRODUCTION

Modern aircraft engines have high turbine inlet temperatures combined with swirl and distorted temperature profile because of combustor cooling, and operation with strong swirl to stabilise flame and enhance the fuel-air mixing. A rotating high-pressure gas turbine is, thus subjected to cyclic thermal and mechanical loads. Shroudless turbine blades have the highest heat load at the tip because of over-tip leakage flows, limiting the life of the engine. Tip loss can account for at least 30% of the losses in stage efficiency [1]. Since the 1970s, numerous causes have been investigated to understand the mechanism of tip leakage flow, and various mitigation techniques have been adapted. However, most of these studies are based on linear cascade or conducted at low-speed rotation due to the high cost of the experiments and difficulty in instrumentation at engine conditions. The capability of OTRF (Oxford Turbine Research Facility) to operate at engine representative conditions, with high-speed rotation and inlet temperature profiles representative of combustor exit flow, gives insight into the effect of rotation and temperature traverse migration.

Figure 1, taken from Yosino (2002), illustrates tip burnout in a high-pressure turbine rotor after in-service operation [1]. The damage can be seen concentrated at the trailing edge pressure side of the blade. The present literature gives two possible reasons: (1) As the airfoil gets thinner towards the trailing edge, it gets difficult to get sufficient cooling flows compared to the rest of the blade and (2) Temperature traverse migration (also termed as hot gas migration). Sharma and Stetson (1998) explained that temperature distortions in the combustor exit flows can change rotor relative inlet conditions [2]. A maximum to minimum temperature ratio of 1.7 at low flow coefficient can make up to 40° difference in relative inlet angles for the hot and cold gas. At high positive incidence, the hot fluid impinges on the pressure side of the airfoil. Combined with buoyancy effects and pressure gradients, the hot spot moves along the pressure surface and in radial direction causing high heat transfer in the late pressure side region at the blade tip.

Blade tip heat transfer is, hence, a key area of research for HP turbine design and cooling. A variety of tip designs at different tip gaps and inlet conditions were tested in the OTRF. The focus of this paper is to present the commissioning of the turbine for these experiments, and highlight the best practices and considerations around heat transfer data obtained using high-frequency response thin-film gauges.



**FIGURE 1: HP TURBINE SQUEALER TIP BLADES AFTER IN-SERVICE OPERATION [1]**

## 2. THE OXFORD TURBINE RESEARCH FACILITY

Experiments for this study were conducted in the OTRF, a short duration transient test facility used for taking unsteady aerodynamic and heat transfer measurements at engine representative conditions. Hilditch et al. [3] first described the design and working of the test facility. The OTRF is capable of matching aerodynamics and heat transfer relevant non-dimensional parameters such as Mach number, Reynolds number, gas-to-wall temperature ratio, turbulence intensity and non-dimensional speed. The schematic of the facility as shown in Figure 2, consists of four main sections: (1) a lightweight piston, (2) a fast-acting plug valve, (3) a working section, and (4) an exhaust tank. Prior to a run, the working section is evacuated until a pressure of ~ 10 mbar is achieved. The rotor is spun at the design rotational speed using an air motor. In the meantime, the piston tube is filled with an initial volume of 10 m<sup>3</sup> air. The piston is moved by compressed air fed from a high-pressure reservoir. The test gas in front of the piston undergoes almost isentropic compression until the desired stagnation pressure and temperature conditions are reached. Subsequently, a fast-acting plug valve is opened to allow the hot gas to flow into the working section. Area of the second throat at stage exit can be varied to tune the rotor exit pressure in order to achieve the required stage pressure ratio and mass flow rate. Choking the flow isolates the turbine from any downstream disturbances. A turbo-brake, downstream of the second throat, is connected to the rotor shaft in order to maintain a constant rotor speed during the stable portion of the run that lasts approximately 400 ms.

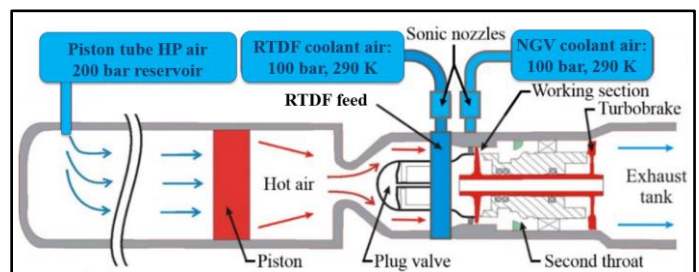


**FIGURE 2: SCHEMATIC OF THE OXFORD TURBINE RESEARCH FACILITY**

Figure 3 shows how NGV (Nozzle Guide Vane) inlet total pressure data can be used to calculate the aerodynamically stable portion of the run (marked by vertical dashed lines). A trapezoid is fit using a linear combination of Heaviside step function and non-linear squares method to find the time period during which the NGV inlet total pressure is stable. A variety of stage inlet temperature profiles including radial distortion and swirl can be produced in the OTRF. For the present investigation, the rig was operated at two different inlet temperature profiles, namely: (1) Uniform i.e., a spatially constant total temperature at stage inlet and (2) RTDF (Radial Temperature Distortion Factor) i.e., a radially varying total temperature at the stage inlet representative of a lean burn combustor exit temperature profile.

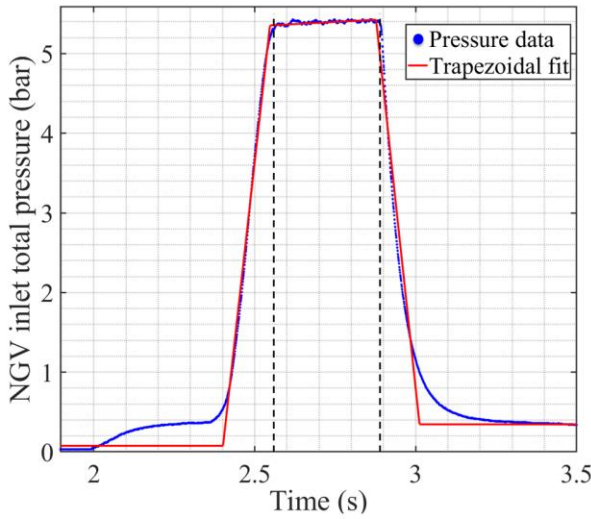


**FIGURE 3:** USE OF NGV INLET TOTAL PRESSURE TO CALCULATE AERODYNAMICALLY STABLE PORTION OF A RUN IN THE OTRF. VERTICAL LINES MARK THE STABLE PORTION OF THE RUN.

#### *Turbine details*

Figure 4 shows schematic of meridional view of the single stage SILOET turbine employed for the current investigation in the OTRF. Shahpar et al. [4] detail the high-fidelity design optimization carried out to develop the SILOET turbine with significantly improved aerodynamic performance to reduce the losses produced by lean burn combustion. The turbine features a subsonic NGV exit and transonic rotor with 50% reaction. The annulus lines in the OTRF are geometrically scaled from a modern civil engine. The turbine consists of 40 cooled NGVs (featuring both film cooling and trailing edge slot cooling), and 60 uncooled rotor blades. Static and total pressure and temperature measurements were taken at various locations in the rig including the planes shown in Figure 4 to monitor the turbine operating conditions and to provide the boundary conditions for CFD simulations. The turbine operating conditions are discussed further in section 2.3.

#### *Flows in the OTRF*

For the purpose of this study, there are three flows of interest in the OTRF: (1) Hot stream i.e., the compressed air that flows into the working section upon opening of the plug valve, (2) Cold stream i.e., the cold air required to generate the RTDF temperature profile at NGV inlet and (3) NGV cooling flow i.e., the cold air required for film and trailing edge slot cooling of the NGV. The RTDF cold stream and NGV cooling flow are introduced in the rig from two independent reservoirs as shown in Figure 2. After leaving the reservoir, the metered RTDF cold stream flow passes through a coolant feed system and is distributed into the hub and casing plenums in the working section. The hub and casing feed rings have a system of choked radial holes that can be systematically blocked to achieve the desired split of mass flow rate. During commissioning, hub-to-casing mass flux ratio was tuned to achieve the desired radial temperature profile. The NGV cooling flow is metered separately and fed from a separate plenum in the outer casing of the working section. The cooling flows are released in the working section prior to the opening of plug valve. This results in a slight rise in NGV inlet total pressure at  $t = 2s$  as can be observed in Figure 3.

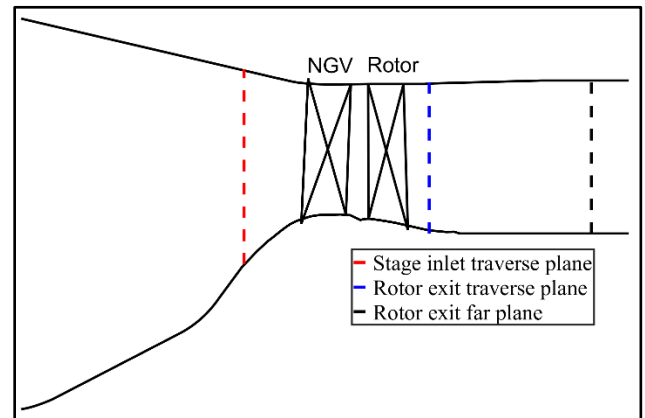


**FIGURE 4:** MERIDIONAL VIEW OF SINGLE STAGE SILOET TURBINE SHOWING AXIAL MEASUREMENT PLANES.

#### **2.1 Mass flow rate measurement**

This section discusses how mass flow rate was calculated for different flows in the OTRF. Figure 5 shows the meridional view of the piston-tube exit contraction with the hot-stream mass flow rate measurement instrumentation. At the fully opened position, the plug valve contraction acts as a converging-diverging venturi. Equation (1) below gives the 1D isentropic mass flow rate for a compressible flow:

$$\left(\frac{dm}{dt}\right)_{1D} = P_0 A_{geo} M \sqrt{\frac{\gamma}{RT_0}} \left(1 + \frac{(\gamma - 1)}{2} M^2\right)^{-\frac{(\gamma + 1)}{2(\gamma - 1)}} \quad (1)$$

Total pressure upstream of the piston-tube exit contraction was measured at four positions on the end-wall of the piston tube using CTE8000 Sensor Technics transducers with a nominal accuracy of 0.05% [5]. The throat was instrumented with four

differential pressure measurements using BTEM5000 Sensor Technics low-pressure transducers. Hence, a time-varying Mach number can be calculated. The location of downstream static pressure tappings was optimised through CFD by Beard et al. [5]. The aim was to maximise the pressure difference with a constraint of having the tappings in a region of accelerating flow to avoid unsteadiness due to flow separation. The total temperature was measured immediately downstream of the contraction. Given a low Mach number of  $\sim 0.05$  in the temperature measurement plane, fast response bare bead  $12.7 \mu\text{m}$  k-type thermocouples were used. To account for non-uniformity and displacement effect of viscous boundary layers, a discharge coefficient can be defined as the ratio of effective area ( $A_{eff}$ ) to geometric area ( $A_{geo}$ ) of the piston tube contraction. The actual mass flow rate therefore is evaluated using Equation (2). The effective area is a function of throat Reynolds number, Mach number, Prandtl number and gas to wall temperature ratio. Beard et al. calibrated the ratio of effective area to geometric area over a range of Mach number and Reynolds number. A plane can be fitted to the calibration data using the least squares method with a standard deviation of  $\pm 0.30\%$  [5]. Effective area for the current operating conditions was calculated by linearly interpolating the calibration data. Beard [5] calculated the bias and precision uncertainty in the hot stream mass flow rate to be 1.4% and 0.2% respectively.

$$\left(\frac{dm}{dt}\right) = \left(\frac{dm}{dt}\right)_{1D} \frac{A_{eff}}{A_{geo}} \quad (2)$$

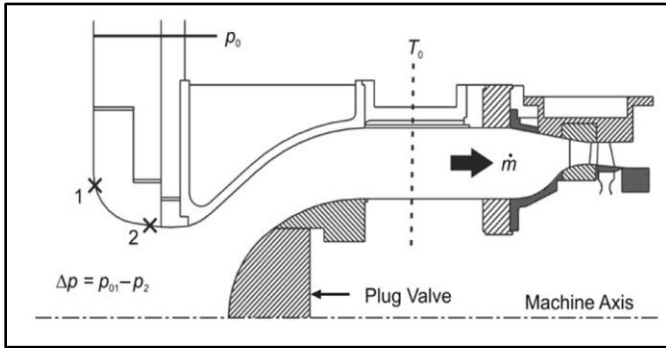


**FIGURE 5:** OTRF PISTON-TUBE EXIT CONTRACTION SHOWING MASS FLOW MEASUREMENT INSTRUMENTATION [5]

Mass flow rate for the RTDF cold stream and NGV cooling flow is controlled using a calibrated sonic venturi nozzle downstream of each of the reservoirs. Using the nozzle upstream total temperature and total pressure, nozzle diameter and discharge coefficient, and in accordance with ISO 9300, mass flow rate for RTDF cold stream and NGV cooling flow can be determined. Figure 6 illustrates the hot stream, cold stream and NGV cooling mass flow rates for a typical RTDF run. The unsteadiness in hot stream mass flow rate corresponds to fluctuations in stage inlet total pressure caused by piston oscillations at  $\sim 16$  Hz and reflection of pressure wave travelling

through the facility at  $\sim 70$  Hz. Beard [5] calculated the bias and precision uncertainty in the cold stream mass flow rate to be  $\pm 0.7\%$  and  $\pm 0.2\%$  respectively.

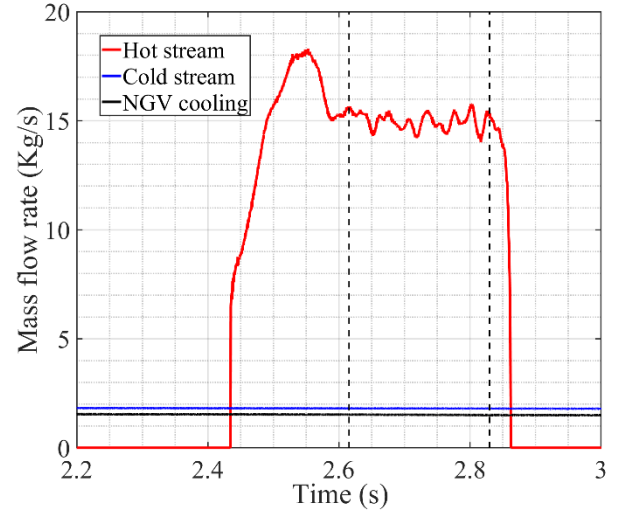


**FIGURE 6:** TIME-INSTANTANEOUS HOT STREAM, COLD STREAM AND NGV COOLING MASS FLOW RATES DURING A TYPICAL RTDF RUN IN THE OTRF.

## 2.2 Mass-averaged NGV inlet total temperature

Stage inlet total temperature can be calculated using a mass-mean of the hot stream and RTDF cold stream flows. However, convective heat transfer to the rig components, upstream of the NGV, can lead to discrepancies in the temperature values between the measurement location that is upstream and the location of interest at inlet to the NGV. The cold stream is delivered at ambient temperature i.e. at very similar temperature to the supply feeds and ejection slots. Hence, the convective heat transfer to the rig components is negligible as no temperature difference exists between the cold stream at the NGV inlet and ejection slots where the temperature is measured. However, the large temperature difference between the hot stream ( $\sim 530$  K) and rig components ( $\sim 290$  K) can cause significant convective heat transfer and hence, a reduction in the hot stream temperature from the upstream measurement location to the NGV inlet plane. Adams et al. [6] developed a non-dimensional heat loss factor ( $\theta$ ), defined according to Equation (3), to account for heat loss by convection to the upstream rig components.

$$\theta = \frac{T_{01} - T_{0h}}{T_w - T_{0h}} \quad (3)$$

Temperature measurements, using hot stream thermocouples and NGV inlet thermocouples, from seven consecutive Uniform runs, were used to calculate the heat loss factor. Stage inlet total temperature ( $T_{01}$ ) is measured using four circumferentially equispaced rakes each consisting of five radially distributed thermocouples. Wall temperature ( $T_w$ ) of the rig was measured for each run. Hot stream temperature ( $T_{0h}$ ) was measured using six circumferentially equispaced rakes each consisting of five radially distributed thermocouples. The hot



stream thermocouple rake plane is shown in Figure 5. The rakes are fitted with 25.4  $\mu\text{m}$  diameter bare bead thermocouples, to achieve the required frequency response, which also makes them fragile. Any data from failed thermocouples in each rake was therefore discounted. Higher heat loss expected near end-walls, and an uneven distribution of good thermocouples will lead to a span-wise bias in the average value of heat loss factor. Hence, the heat loss factor was first averaged circumferentially at each radial span and then an average of heat loss factor from all spans was taken for each run. Figure 7 illustrates the evaluated heat loss factor as a function of time. The mean from consecutive Uniform runs is calculated and the standard deviation is indicated within the shaded region on the graph. The average value of heat loss factor in the stable portion of the run was found to be 0.1035. Adams et al. reported a heat loss factor of 0.151, a higher value due to the presence of combustor swirlers (and hence, increased area for convective heat transfer) that are not used in the present study.

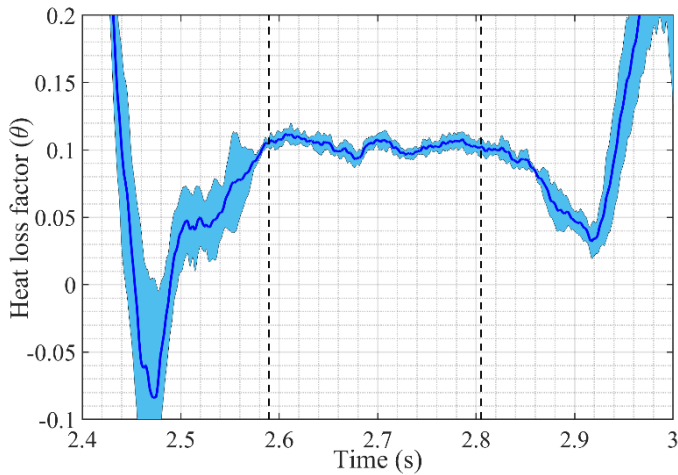


**FIGURE 7:** MEAN OF MEASURED NON-DIMENSIONAL HEAT LOSS FACTOR ACROSS SEVEN UNIFORM RUNS. THE SHADED REGION INDICATES THE STANDARD DEVIATION. VERTICAL LINES MARK THE STABLE PORTION OF THE RUN.

Using measured hot stream temperature ( $T_{oh}$ ), rig wall temperature ( $T_w$ ) and  $\theta = 0.1035$  for a given run, the term  $T_{oi}$  in Equation (3) hence gives the corrected hot stream temperature ( $T_{oh\_corr}$ ). The NGV inlet mass-averaged total temperature is calculated using the corrected hot stream temperature as described by Equation (4). Having prior knowledge of the heat loss factor allows the rig to be operated at a higher compression temperature to achieve the design stage inlet total temperature. Equation (5) gives the mass-averaged rotor inlet total temperature that can be calculated by including NGV cooling flow mass flow rate and temperature in Equation (4). Figure 8 illustrates all these temperature traces during a typical RTDF run in the OTRF.

$$T_{oi} = \frac{m_h T_{oh\_corr} + m_c T_{oc}}{m_h + m_c} \quad (4)$$

$$T_{o2} = \frac{m_h T_{oh\_corr} + m_c T_{oc} + m_{c\_NGV} T_{oc\_NGV}}{m_h + m_c + m_{c\_NGV}} \quad (5)$$

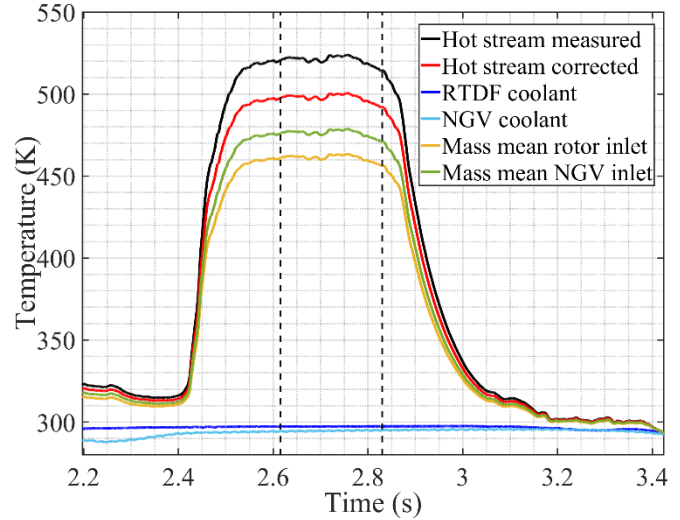


**FIGURE 8:** MEASURED AND CORRECTED TOTAL TEMPERATURE TRACES DURING A TYPICAL RTDF RUN IN THE OTRF

### 2.3 Turbine operating conditions

Table 1 summarizes the turbine operating conditions averaged over 16 runs for each inlet condition. The standard deviation between runs for most parameters is within  $\pm 1\%$  showing a good run to run consistency. The ‘Predicted Uniform’ column in the table lists the values from Q263 (a Rolls-Royce through-flow solver) using design conditions for the Uniform inlet. At the stage inlet of the working section, there are four probes distributed circumferentially at  $90^\circ$  apart, each consisting of 5 pitots, to measure NGV inlet total pressure ( $P_{oi}$ ). Mach number at NGV exit was calculated using measurements from static pressure tapings located at the casing wall region of NGV exit and total pressure measured at stage inlet. The predicted value for NGV exit Mach number is higher than experimental value due to limitations of the through-flow solver such as not accounting for tip gap. Static pressure tapings on the hub and casing walls of the rotor exit can be used to calculate the stage pressure ratio. The rotational speed of the shaft was measured using an optical encoder and is presented as  $N/\sqrt{T_{oi}}$ . Turbulence intensity, not listed in Table 1, was measured in a previous test campaign [7] using hot wire anemometer and was found to be 6.5% at the NGV inlet. The Reynolds number is calculated at NGV exit flow conditions. Nusselt number for turbulent flow over a flat plate is a function of Reynolds number and Prandtl number as expressed by Equation (6) for  $5 \times 10^5 \leq \text{Re} \leq 10^7$  and  $0.6 \leq \text{Pr} \leq 60$ . Using this correlation at NGV exit conditions, an approximate estimate of Nusselt number and its run-to-run variation can be studied. Standard deviation in Nusselt number over multiple runs was found to be within  $\pm 0.6\%$  which shows the capability of the OTRF to repeat flow conditions that allows heat transfer data to be taken over multiple

**TABLE 1: OPERATING CONDITIONS FOR SINGLE STAGE SILOET TURBINE IN OTRF AT UNIFORM AND RTDF INLET TEMPERATURE PROFILES**

Parameter	Predicted Uniform	Measured Uniform		Measured RTDF	
		Mean (16 runs)	% Std. dev. (16 runs)	Mean (16 runs)	% Std. dev. (16 runs)
$T_{01}$ (K)	475	469.4	$\pm 0.23$	472.3	$\pm 0.81$
$P_{01}$ (bar)	5.4	5.397	$\pm 0.32$	5.408	$\pm 0.49$
$P_{01}/P_3$	2.63	2.579	$\pm 0.45$	2.58	$\pm 0.34$
$N/\sqrt{T_{01}}$ (rpm/K)	391.2	392.33	$\pm 0.50$	391.97	$\pm 0.27$
$M_{NGV\_exit}$	0.80	0.75	$\pm 1.06$	0.75	$\pm 0.99$
$Re_{NGV\_exit}$	$1.72 \times 10^6$	$1.69 \times 10^6$	$\pm 0.72$	$1.69 \times 10^6$	$\pm 0.48$
$Nu_{NGV\_exit}$	3185.9	3145.0	$\pm 0.58$	3139.2	$\pm 0.40$
$T_g/T_w$	1.58	1.59	$\pm 0.53$	1.6	$\pm 0.26$
$m_{in}\sqrt{T_{01}/P_{01}}$ (kgK <sup>1/2</sup> /sbar)	70.22	67.38	$\pm 0.37$	67.81	$\pm 0.43$
$m_{c\_NGV}$ (kg/s)	1.5	1.51	$\pm 0.36$	1.51	$\pm 0.29$
$m_c$ (kg/s)	N/A	N/A	N/A	1.815	$\pm 0.53$

runs. For instance, casing heat transfer data is taken by setting different wall temperatures over multiple runs. The data from multiple runs is then combined to increase the range of regression that improves the accuracy of adiabatic wall temperature and heat transfer coefficient calculation.

$$Nu = 0.037 Re^{4/5} Pr^{1/3} \quad (6)$$

### 3. NGV INLET TEMPERATURE PROFILE SURVEY

Hall et al. [8] detailed the design of a non-reacting combustor simulator with swirl and temperature distortion employed in the OTRF. However, this study focuses on comparisons of uniform and radial temperature profiles. Therefore, the swirlers were removed and only annular slots at the hub and casing were used to create a radial temperature profile. Annular slots offer manufacturing advantage and uniform mass flow distribution compared to the use of dilution holes and perforated plates. The inlet total pressure profile is kept radially constant by design. The same hardware is used for the Uniform inlet conditions but the cold stream is not blown from annular slots at hub and casing. The profile is measured one and half NGV axial chords upstream of the NGV leading edge.

The short run time of the OTRF and small time-varying fluctuations in total temperature and pressure arising from piston oscillation makes the use of traverse probes difficult. Hence, the NGV inlet temperature profile survey was conducted using thermocouple rakes that can be sequentially moved both in radial and circumferential direction over multiple runs in the OTRF. Two types of rakes were used: (1) Three primary rakes, each consisting of nine radially distributed thermocouples and (2) Three end-wall rakes, each consisting of two thermocouples near hub and one thermocouple near casing end walls. Three rakes can be used simultaneously by mounting them in a mini cassette that can be inserted into the working section through one of the four removable cassettes as shown in Figure 9. Four mini-cassettes are interchanged to vary the circumferential position.

In addition, the primary rakes can be used in two different radial settings. This system of traverse and radial movement of probes over multiple runs makes 27 x 8 primary rake and 9 x 4 end-wall rake measurements possible. In total, these 252 temperature measurement locations are distributed over two NGV pitches with span-wise coverage of ~ 4% to 98%.

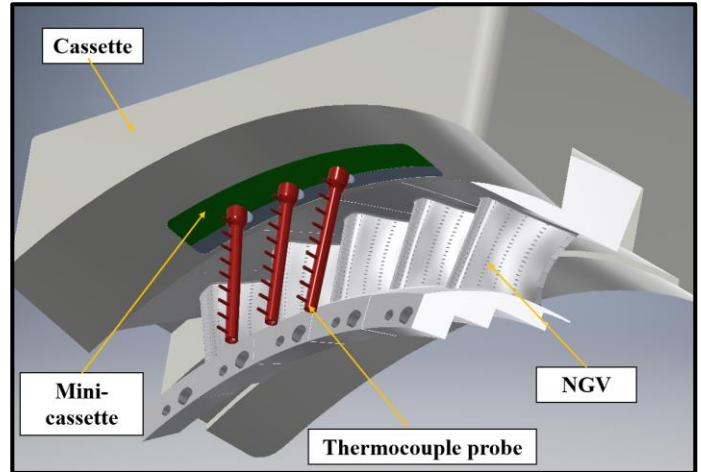


**FIGURE 9: ISOMETRIC VIEW OF NGV INLET TEMPERATURE AREA SURVEY INSTRUMENTATION IN CAD ASSEMBLY**

Bare bead k-type thermocouples used were 25.4  $\mu$ m in diameter. These thermocouples have been validated to provide the transient response required for accurate temperature measurement in the low velocity ( $M \sim 0.1$ ) flow field at NGV inlet. The overall bias and precision uncertainties in the total temperature measurement are  $\pm 0.29\%$  and  $\pm 0.13\%$  respectively [9]. The temperature data from the area survey was non-dimensionalised into total temperature effectiveness ( $T_{0eff}$ ), defined by Equation (7), to account for small variations in hot and cold stream total temperatures over multiple runs.

$$T_{0eff} = \frac{T_{01} - T_{0c}}{T_{0h} - T_{0c}} \quad (7)$$

Figure 10 illustrates the effectiveness contour calculated by interpolating the area survey data. The radial solid lines indicate the hub and casing position, circumferential dashed lines indicate NGV leading edge positions and circles indicate thermocouple measurement locations. A circumferential average of survey data was calculated at each span to produce a radial profile. Figure 11 compares measured radial effectiveness profile with the target profile, representative of a lean-burn combustor exit profile.

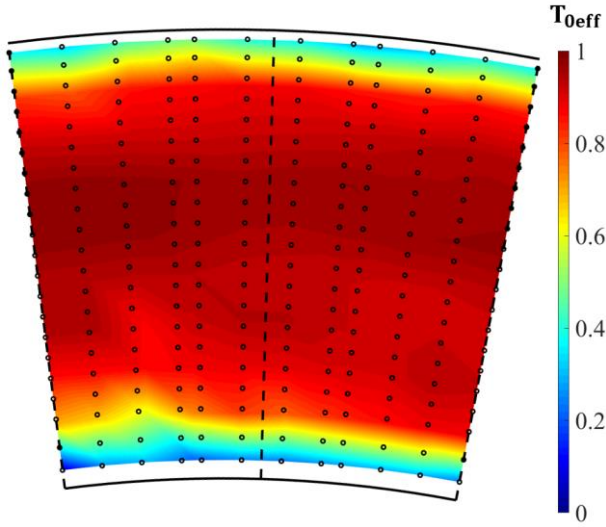


**FIGURE 10:** MEASURED AREA SURVEY EFFECTIVENESS CONTOUR. VERTICAL DASHED LINES MARK THE NGV LEADING EDGE LOCATION. THERMOCOUPLE LOCATIONS ARE SHOWN BY CIRCLES. SOLID LINES AT CONSTANT RADIUS SHOW CASING AND HUB.

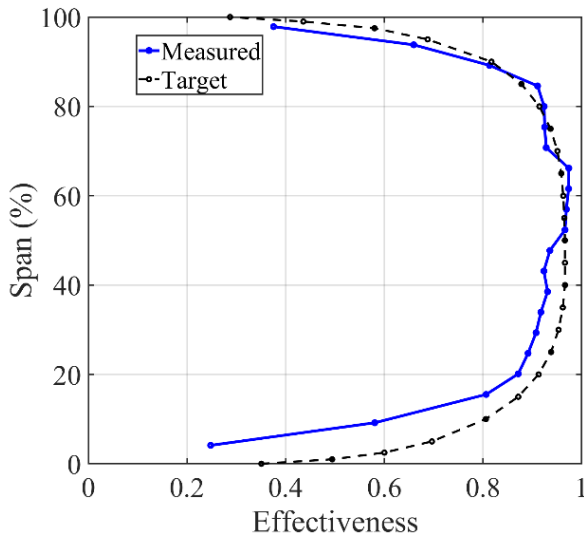


**FIGURE 11:** CIRCUMFERENTIALLY AVERAGED NGV INLET EFFECTIVENESS PROFILE

#### 4. HEAT TRANSFER MEASUREMENT ANALYSIS

The conditions in the engine HP turbine environment make instrumentation difficult due to the elevated temperature and pressure levels. Therefore, measurements in this region are generally unreliable, inaccurate and of poor resolution. Transient facilities like the OTRF allow accurate unsteady aerodynamics and heat transfer measurements possible in an engine representative environment. Annular cascade, high-speed rotation and short run time of the transient facility restricts optical access and makes Infrared/liquid crystal measurements difficult. Heat transfer instrumentation using platinum thin-film gauges overcomes these obstacles. With a frequency response of ~100 KHz, the thin-film gauges are ideal for use in transient facilities like the OTRF and have proven to resolve blade passing frequencies (~10 KHz), and random unsteadiness caused by the turbulent flow [10]. In addition to heat transfer measurements on stationary surfaces such as NGVs, casing and platforms, thin-film gauges can be powered through in-shaft electronics to instrument high-speed rotating turbine blades. This section presents a heat transfer measurement analysis for the use of thin-film gauges covering the theory of operation, latest manufacturing and data-processing techniques, thermal properties of substrates used, parametric study and thermal modelling of the gauge response.

##### *Manufacturing of a thin-film gauge*

Schultz and Jones [11] pioneered the use of thin film gauges as surface resistance thermometers in short-duration facilities. Since 1973, the manufacturing technique for the thin-film gauges has evolved. Collins et al. [12] detailed the latest technique for fabrication of the thin-film gauges. The hand-painting of sensors presented by Schultz and Jones has been developed further through the use of magnetron sputtering and etching of thin-films (< 40 μm) of platinum and copper respectively onto a thermally insulating substrate. Platinum is used because of its high temperature sensitivity and long range of stable linear temperature-resistance dependence governed by Equation (8).

$$R = R_o (1 + \alpha_{cal} \Delta T) \quad (8)$$

The choice of thermally insulating surface depends on the application, and constraints imposed by the geometry and mechanical strength requirements. In the past, Macor (a machinable glass ceramic) has been used with platinum directly painted onto the insulating surface. However, structural requirements at high-speed rotation necessitate the use of metallic turbine blades. A flexible sheet of a polyimide (Kapton) pre-laminated with copper can be etched to create electrically conducting copper tracks. With a copper thickness of 18 microns, this technique helps in decreasing the required width of copper tracks leading to a five-fold increase in lateral gauge density [12]. Post photo-fabrication of copper tracks and sputtering of platinum, the polyimide sheet can be pasted on a metallic surface such as turbine blades, as shown in Figure 12a, using high performance 3M film adhesive.



Piccini et al. [13] calibrated the thermal properties and thickness to thermal conductivity ratio of the insulating top layer (polyimide and adhesive) using a shutter rig experiment. It was found that the adhesive sheet and polyimide sheet had the same thermal product value ( $\sqrt{\rho C_p k} = 490$ ) with a measurement uncertainty of 4.2%. Hence, the polyimide-adhesive package has been treated as a single top layer substrate and metal blade as the bottom layer substrate for the heat transfer analysis. The combined polyimide-adhesive package is henceforth referred as polyimide in the paper.

#### Sensitivity of a thin-film gauge

Converting Equation (8) into voltage and differentiating with temperature gives Equation (9) that represents the sensitivity of a thin-film gauge (where  $\rho_r$ ,  $l$  and  $w$  are respectively the electrical resistivity, length, and width of the thin film,  $I_e$  is the gauge excitation current, and  $\alpha_{cal}$  is the temperature coefficient of resistance). A thin, high resistivity and high length-width ratio thin-film gauge is desirable for good voltage-temperature sensitivity. The design and dimensions of the thin-film gauges have been optimised through numerous studies carried out at Oxford [11,12,14]. Serpentine gauges developed by Collins [12] were found to give erroneous measurements due to strain effects coupled with temperature effects. Straight gauges, as shown in Figure 12b, with length-to-width ratio of 10 and a large overlap with the copper tracks have proven to show the highest sensitivity, low strain effect, high strength, high gauge density (spatial resolution) and consistent temperature coefficient of resistance during calibration (20 to 80°C).

$$\frac{\partial V}{\partial T} = \frac{\rho_r l}{wt} \alpha_{cal} I_e \quad (9)$$

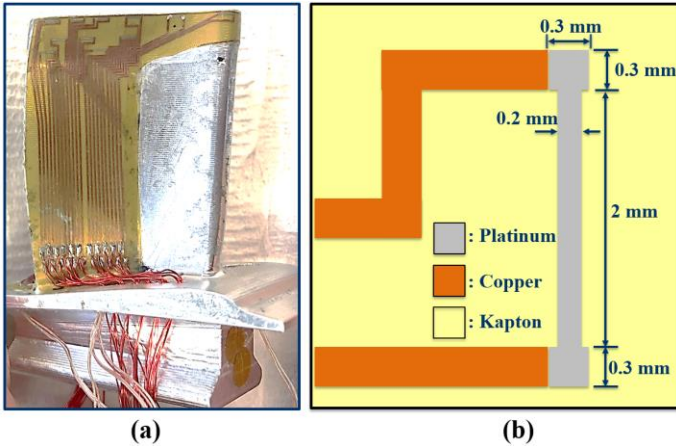


**FIGURE 12:** THIN-FILM GAUGE INSTRUMENTATION: (A) POLYIMIDE SHEET ON AN ALUMINIUM HP ROTOR BLADE SHOWING PHOTO-FABRICATED COPPER TRACKS AND SPUTTERED PLATINUM GAUGES, (B) LAYOUT OF A SINGLE THIN-FILM GAUGE

#### Calibration of thin-film gauges

The temperature coefficient of resistance ( $\alpha_{cal}$ ) for a thin-film of platinum is much lower than bulk platinum because of a reduction in the mean free path of electrons in the thin-film [15]. In addition, the thin film can get stretched upon pasting the polyimide sheet on the rotor blade surface (especially towards the early suction side where the aerofoil typically has a high curvature). Hence, the resistance of each thin-film gauge needs to be calibrated against temperature. After pasting the polyimide sheet on the metal substrate such as a rotor blade, the specimen is passed through multiple cycles of annealing the thin-film gauges to release any stresses and enhance the chemical stability of the sputtered platinum. The thin-film calibration facility at Oxford consists of a thermostatically controlled water bath (a heater and chiller with capability to vary the bath temperature from 5°C to 95°C), a National Instruments PXI system, and a workstation with LabVIEW program [12]. A 22-bit National Instruments DMM with 96 thin-film channels measures the gauge resistance with a resolution of 1 mΩ. The temperature of the water bath and specimen is monitored using thermocouples, and once an equilibrium (with set tolerances) is achieved, temperature and gauge resistance values are recorded. The whole process is automated to pass through 8 cycles from 25°C to 75°C in steps of 5°C. Multiple passes are necessary to check for hysteresis and obtain substantial calibration data for a good linear fit. Figure 13 shows calibration data and corresponding linear fit along with 95% confidence interval for a typical thin-film gauge on a rotor blade. Most gauges were found to give a temperature coefficient of resistance ( $\alpha_{cal}$ ) value of  $\sim 1 \times 10^{-3}/^\circ\text{C}$  which is less than the value for bulk platinum ( $\alpha = 3.9 \times 10^{-3}/^\circ\text{C}$ ) as explained earlier [15].

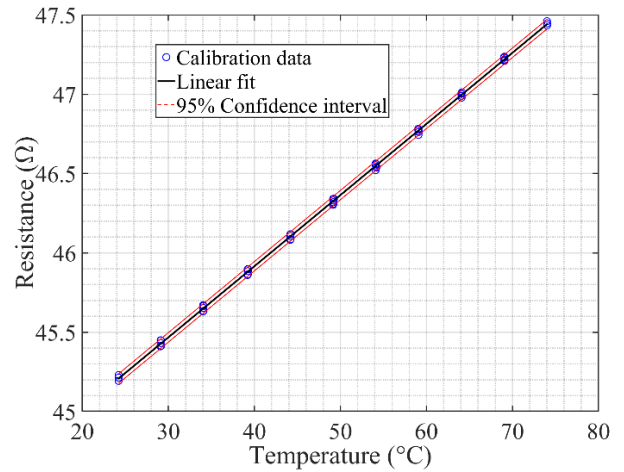


**FIGURE 13:** CALIBRATION OF RESISTANCE AGAINST TEMPERATURE FOR A TYPICAL THIN-FILM GAUGE ON ROTOR BLADE

Using the offset data and temperature coefficient of resistance ( $\alpha_{cal}$ ) obtained from the calibration, voltage from a thin-film gauge can be converted into temperature while keeping the current constant. The blue trace in Figure 14 shows a typical temperature rise of thin-film gauge on a rotor surface during a run of the OTRF. By varying the  $\alpha_{cal}$  value by  $\pm 10\%$ , two more



temperature traces are calculated from the same voltage signal and shown in Figure 14. A positive correlation is observed: increasing the  $\alpha_{cal}$  by 10% increases the temperature rise of the given thin-film by 8.3% while decreasing the  $\alpha_{cal}$  by 10% decreases the temperature rise of the given thin-film by 6.8%. Post-calibration, the temperature coefficient of resistance was found to vary by  $\sim 9\%$  between thin-film gauges at same location on the blade but sputtered in different batches, indicating the effect of having small differences in the thickness of sputtered platinum. In addition, the temperature coefficient of resistance between two thin-film gauges instrumented at leading edge and trailing edge of the same blade was found to vary by  $\sim 6\%$ . This indicates the effect of stretching of thin-film gauge in the region of high curvature towards the leading edge of the blade. Hence, it is essential to calibrate all thin-film gauges after pasting the polyimide sheet on the metal substrate before each experimental test campaign.

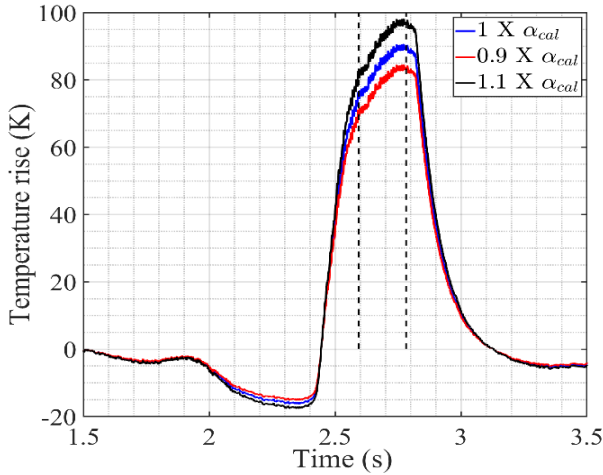


**FIGURE 14:** TEMPERATURE RISE CALCULATED FROM A SINGLE VOLTAGE SIGNAL DURING A RUN IN THE OTRF WITH DIFFERENT TEMPERATURE COEFFICIENT OF RESISTANCE.

#### *Semi-infinite single layer substrate*

Using 1D heat conduction Equation (10) and assuming a single layer of semi-infinite substrate, Equation (11) can be derived which shows that given the surface temperature history from a thin-film gauge, surface heat flux can be calculated.

$$\frac{\partial^2 T}{\partial x^2} = \frac{1}{\alpha} \frac{\partial T}{\partial t} \quad (10)$$

$$\dot{q}_s = \sqrt{\frac{k\rho C_p}{\pi}} \left( \frac{T_s(t)}{\sqrt{T_s}} + \int_0^t \frac{T_s(t) - T_s(\tau)}{(t - \tau)^{3/2}} d\tau \right) \quad (11)$$

However, it is essential to understand when the semi-infinite assumption breaks down in order to calculate the minimum required thickness of the insulating substrate (Polyimide-adhesive package in this case). Figure 15 plots the temperature and heat flux, each normalised by its respective surface values,

against non-dimensional penetration depth ( $x^*$ ) for a constant surface heat flux boundary condition. Temperature and heat flux reach 1 % of their respective surface values at  $x^* = 1.58$  and 1.87. Schultz and Jones [11] recommended using  $x^* = 1.58$  for the semi-infinite assumption to be valid. Given the 0.5 s run time of the OTRF, a substrate layer of  $\sim 600$  microns is required for the semi-infinite assumption to be valid. This thickness value can be achieved easily when instrumenting a geometry such as the casing segment of the turbine with thin-film gauges. However, flexibility of the polyimide sheet (air bubbles get trapped in regions of high geometric curvature) and the risk of a thicker polyimide sheet peeling off due to the increased weight, high-speed flow and centrifugal forces restrict the thickness on NGVs and particularly on rotating surfaces such as rotor blade aerofoil and platform.

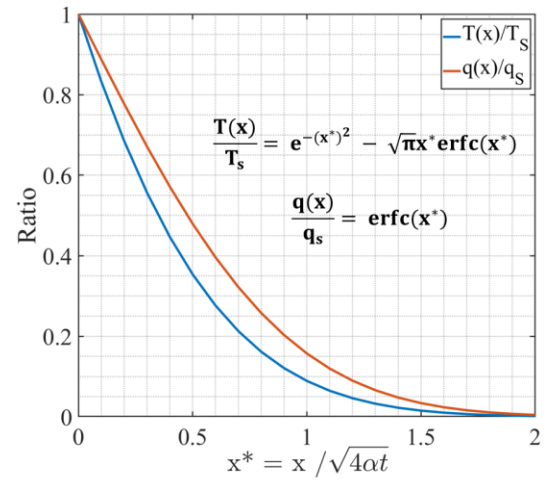


**FIGURE 15:** NORMALISED SURFACE TEMPERATURE AND HEAT FLUX TRACES FOR A CONSTANT SURFACE HEAT FLUX CASE, SHOWING NON-DIMENSIONAL PENETRATION DEPTH

#### *Multi-layer substrate*

Double-sided thin-film gauges developed by Usandizaga [14] feature a second thin-film several microns below the surface thin-film. This provides an additional temperature boundary condition that can be used to solve the 1D heat conduction equation without the semi-infinite assumption. However, the addition of a second thin-film gauge comes with an additional layer of polyimide and adhesive layer, that adds to the combined package making it bulky and heavy. A further factor which makes the double-sided gauges undesirable is the complexity of connecting leads to the underside gauges. A Direct Heat Flux Gauge developed by Piccini et al. [13] uses a combination of thin-film gauge and thermocouple as shown in Figure 16b. A bare-bead and fine-wire (0.075 mm diameter) k-type thermocouple can be flush-fitted to the airfoil surface in contact with the polyimide sheet. Given the high thermal conductivity of Aluminum, relatively few thermocouples underneath the polyimide provides a good estimate of the metal temperature [13].

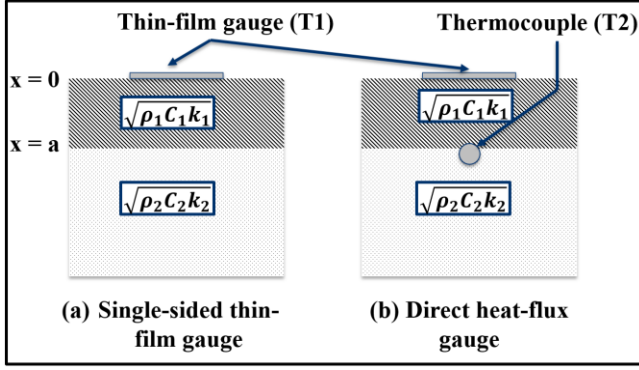


**FIGURE 16: TWO THIN-FILM GAUGE CONFIGURATIONS**

#### Heat flux processing technique

Analytical solution for heat flux, such as Equation (11), can be derived easily for a 1D semi-infinite single-layer substrate. However, the thickness limitations on the polyimide requires a two-layer analysis. Doorly and Oldfield [16] first described the theory behind the use of thin-film gauges for multi-layered substrates. Equations for two-layer substrates are more complicated and require numerical approximations to the solutions of the linear differential equations. Oldfield [17] later developed a new method based on an impulse response technique to compute heat flux from the temperature history for a variety of thin-film gauge configurations. Figure 17 summarises the impulse response method in a flow chart. Given a gauge configuration and a known analytical solution (such as response to a constant surface heat flux), an impulse response to the system can be computed. The output (heat flux in this case) for a given input (measured temperature at the surface and/or polyimide-metal interface for example) to a linear time-invariant system can be derived as the convolution integral of the input and its impulse response. This is achieved with MATLAB using the FFT (Fast Fourier Transform) based filtering. Oldfield [17] reported that the impulse response method is more accurate and faster than previous methods for heat flux processing.

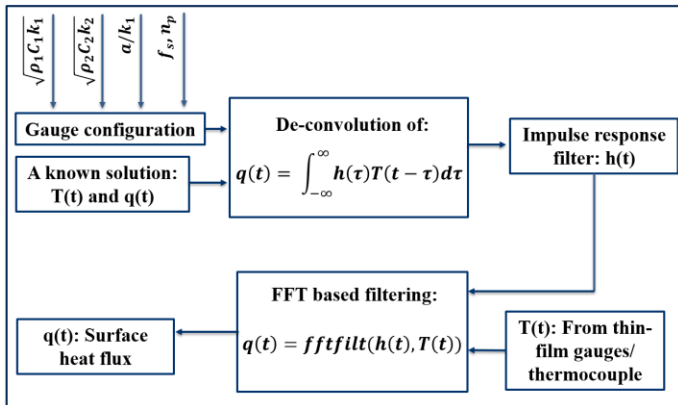


**FIGURE 17: FLOW CHART FOR PROCESSING HEAT FLUX USING THE IMPULSE RESPONSE METHOD**

Figure 18 shows a raw temperature trace, during a typical run in the OTRF, from a thin-film gauge installed on a casing

segment of a HP turbine. The raw temperature data was smoothened in MATLAB using a moving average filter that creates a series of averages using 1% of the data points in the whole data set. Both these temperature traces are then processed through the impulse response method to generate corresponding raw and smooth heat flux traces as shown in Figure 18. Numerical differentiation amplifies the measured unsteadiness in temperature during the impulse response processing and hence, the raw heat flux trace shows significantly higher fluctuations than the raw temperature trace.

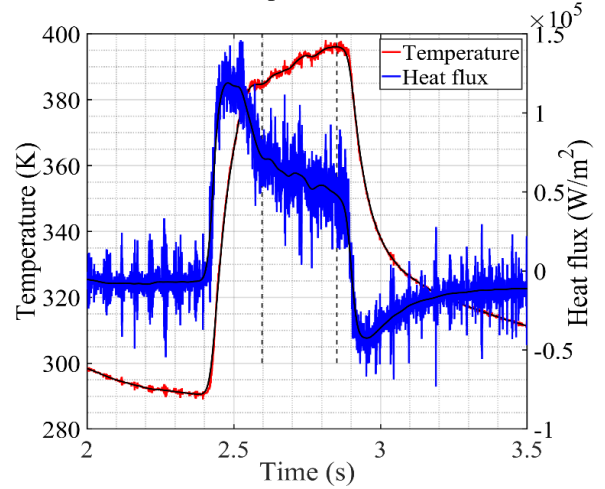


**FIGURE 18: TEMPERATURE AND HEAT FLUX TRACES DURING A TYPICAL RUN IN THE OTRF FROM A THIN-FILM GAUGE INSTALLED ON THE CASING SEGMENT**

#### 4.1 Parametric study of heat flux

A parametric study was performed to understand the sensitivity of heat flux processed using the impulse response method. Figure 17 shows the parameters on which the impulse response filter ( $h$ ) depends. As discussed in the previous section, heat flux is processed from the time history of a thin-film gauge temperature rise using the FFT (Fast Fourier Transform) based impulse response filtering technique. The sampling frequency ( $f_s$ ) and total number of samples ( $n_p$ ) are user-specified and fixed for a given trace. The sensitivity of heat flux to the remaining parameters i.e., thermal product of polyimide ( $\sqrt{(\rho C_p k)_1}$ ), thermal product of aluminium ( $\sqrt{(\rho C_p k)_2}$ ) and thickness to thermal conductivity ratio ( $a/k_1$ ) of polyimide is discussed in this section. Each of these 3 parameters were varied by  $\pm 10\%$  while keeping the other two parameters at the nominal values while the effect on heat flux was studied. Heat flux in all the cases is calculated using temperature data from the same thin-film gauge and two-layer semi-infinite method.

Table 2 summarises the material properties of polyimide and aluminium 7075-T6 alloy (material used for the rotor blades). The thermal product of polyimide was calibrated by Piccini et al. [13] using a set of shutter rig experiments. Figure 19a illustrates the change in heat flux with a change in the thermal product value of polyimide. A positive correlation is observed with a maximum change of  $\pm \sim 11\%$  in heat flux as the mainstream flow is established. This difference in heat flux diminishes towards

the latter part of the run as the thermal pulse conducts through the polyimide layer. However, the same change of  $\pm 10\%$  in thermal product of the aluminium substrate produces only  $\sim \pm 0.03\%$  change in heat flux, as shown in Figure 19b. This demonstrates the weak dependence of heat flux on the thermal properties of the bottom substrate layer.

**TABLE 2: MATERIAL PROPERTIES OF SUBSTRATES USED IN THE HEAT TRANSFER MEASUREMENT ANALYSIS**

Material property	Polyimide (Kapton)	Aluminium 7075-T6
Density ( $\text{Kgm}^{-3}$ )	1420	2810
Thermal conductivity ( $\text{Wm}^{-1}\text{K}^{-1}$ )	0.12	130
Specific heat capacity ( $\text{JKg}^{-1}\text{K}^{-1}$ )	1090	960
Thermal product, $\sqrt{\rho C_p k}$ ( $\text{Wm}^{-2}\text{K}^{-1}\text{s}^{0.5}$ )	490	18727

The Impulse response technique generates the filter using the ratio of thickness to thermal conductivity ( $a/k_1$ ) of polyimide as a single value rather than individual values. Figure 19c illustrate the change in heat flux due to  $\pm 10\%$  change in the thickness to thermal conductivity ratio. Firstly, a difference starts appearing at  $\sim 0.1\text{s}$  after the run starts and continues to increase until the end of the stable portion of the run. This shows the difference in time taken by the thermal pulse to travel through the polyimide layer and reach the start of the aluminium substrate. The thermal conductivity of polyimide was calibrated by Piccini et al. [13] using a set of shutter rig experiments. However, the thickness of the top layer substrate may vary due to stretching of adhesive film. The results can therefore be inferred as: a 10% increase in thickness of polyimide causes the heat flux to fall by 6.8% compared to the nominal case while a 10% decrease in polyimide thickness causes the heat flux to rise by 9.1% compared to the nominal case. Hence, the accuracy of the thermal product and thickness of polyimide is necessary to

get good quality heat flux results using the Impulse response method.

## 4.2 Uncertainty analysis

Oldfield [17] reported the errors in heat flux due to impulse response processing to be negligible and the mathematical accuracy to be dependent on the rounding errors of the processing tools used. MATLAB was proven excellent in this regard with errors less than  $\pm 6 \times 10^{-14}$  for a unit heat flux when processed from a parabola in surface temperature. The overall accuracy of the heat flux, hence, depends on the accuracy of the inputs to the impulse response filter and accuracy of measured temperatures. Kline and McClintock [18] describe the total probable uncertainty for a dependent parameter as the square root of the summed squares of uncertainties of all independent parameters given the component uncertainties are estimated at the same confidence interval. This approach involves calculation of partial derivatives of the parameter with respect to all the independent variables. Often it is difficult to obtain these partial derivatives because of the complex functional relationship such as in the case of impulse response processing. Moffat [19] described a ‘jitter analysis’ in which each independent variable is perturbed and the effect on the final parameter is calculated. The total probable uncertainty for heat flux can therefore be calculated using Equation (12) where  $C_i$  (termed sensitivity coefficient) is defined as the percentage change in heat flux with 1% change in the given parameter. The percentage change in heat flux is evaluated as an average percentage change in the stable portion of a run in the OTRF.

$$\frac{\sigma_q}{q} = \sqrt{(C_1 \sigma_{T_w})^2 + (C_2 \sigma_{(\sqrt{\rho C_p k})_1})^2 + (C_3 \sigma_{(\sqrt{\rho C_p k})_2})^2 + (C_4 \sigma_{(a/k_1)})^2} \quad (12)$$

Table 3 summarises the component uncertainty along with the sensitivity coefficient. The uncertainty in thin-film gauge

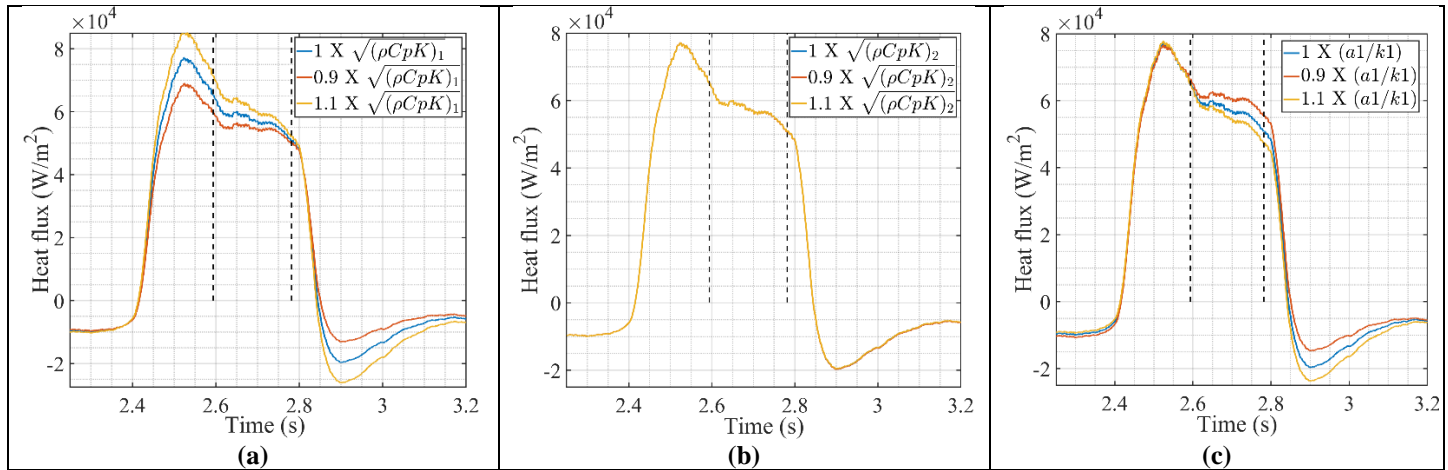


**FIGURE 19: PARAMETRIC STUDY FOR HEAT FLUX: (A) EFFECT OF  $\pm 10\%$  CHANGE IN THERMAL PRODUCT OF POLYIMIDE, (B) EFFECT OF  $\pm 10\%$  CHANGE IN THERMAL PRODUCT OF ALUMINIUM, (C) EFFECT OF  $\pm 10\%$  CHANGE IN THICKNESS TO THERMAL CONDUCTIVITY RATIO OF POLYIMIDE**



temperature rise propagates from: (1) temperature coefficient of resistance (0.9%, using 95% confidence interval on the slope and intercept of calibration line shown in Figure (13)) and (2) offset temperature data of the thin-film gauge (0.4%). The thermal product of aluminium alloy is known accurately and contributes negligible to the uncertainty of heat flux with a very low sensitivity coefficient. Thermal properties of polyimide were calibrated to 4.2% accuracy by Piccini [13], and are major contributors to the uncertainty in heat flux. The overall uncertainty in heat flux was calculated to be 3.3% for both semi-infinite two-layer substrate and direct heat flux gauge configuration ( $\pm 1.1$  K uncertainty in thermocouple measurement was found to have negligible effect on heat flux uncertainty because of low sensitivity coefficient for the interface temperature).

**TABLE 3: SOURCES OF UNCERTAINTY IN HEAT FLUX**

Parameter	Uncertainty ( $\sigma_i$ ), % (95% confidence interval)	Sensitivity coefficient ( $C_i$ )
Thin-film gauge temperature, $T_w$	1.0	1
Thermocouple temperature, $T_2$	0.4	-0.02
Thermal product of polyimide, $\sqrt{(\rho C_p k)_1}$	4.2	0.48
Thermal product of aluminum, $\sqrt{(\rho C_p k)_2}$	0.5	0.003
Thickness to thermal conductivity ratio, $a/k_1$	4.2	-0.56

### 4.3 Thermal modelling

The heat transfer analysis in the previous section considered heat conduction in one-dimension through multiple layers of substrates, polyimide and aluminium. The analysis does not account for: (1) three-dimensional diffusion of heat to the substrate, (2) side-conduction i.e., the additional heat, conducted from surfaces other than the instrumented surface, that travels through the substrate(s) and may affect a thin-film or thermocouple measurement. As shown in Figure 12a, the squealer tip rotor blades for this study were instrumented with thin-film gauges on the aerofoil pressure and suction surface in the near tip region. These thin-film gauges and the thermocouples underneath the polyimide sheet are likely to be affected by heat conduction from the squealer cavity top surface, squealer rim tip and squealer rim inner wall. Hence, a thermal model was developed to: (1) model the diffusion of thermal pulse through multi-layered substrate, (2) quantify the side-conduction effects. The thermal analysis was initiated with a point heat source in 1D domain and, subsequently a line heat source in a 2D domain, and finally an area heat source in a 3D domain.

#### Numerical setup

For the 3D thermal model, a cube of 40 x 40 x 40 mm dimensions was designed. The edge length of the cube was

chosen to be representative of the rotor blade span. A squealer rim was added onto one edge of the cube as shown in Figure 20. The dimensions of the squealer rim were chosen to predict the worst-case scenario of maximum side-conduction, which corresponds to the minimum squealer rim width of the rotor blade. The outer rim side surface of the cube was extended to a variety of thicknesses to model the effect of the polyimide layer thickness. The geometry was meshed using ANSYS workbench meshing tool. The squealer rim was resolved into 25 prismatic layers with a further refinement of 40 prism layers within the polyimide. Nusselt number, from previous OTRF rotor heat transfer measurements, was scaled for the current Reynolds number to evaluate a heat transfer coefficient. This was used as a convection boundary condition for the thermal model. To study the effects without side-conduction, only the surface of polyimide exposed to the gas path (squealer rim outer wall) was subjected to a convection boundary condition and the remaining surfaces were set to an adiabatic wall condition. The driving gas temperature was set to 421 K i.e., the design rotor relative temperature at the tip. The initial temperature of the squealer cube domain was set to 290 K. Second order upwind scheme was used to solve the energy equation in ANSYS Fluent. The solution was solved using a first order implicit transient scheme. The computation was run for 0.5s to match the OTRF run time.

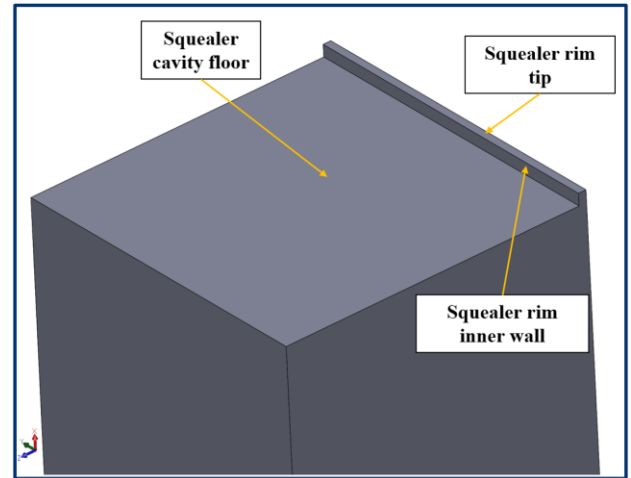


**FIGURE 20: ISOMETRIC VIEW OF THE SQUEALER CUBE DOMAIN MARKED WITH THE SURFACES EXPOSED TO FLOW AND RESPONSIBLE FOR SIDE-CONDUCTION.**

#### Comparison with 1D analytical solutions

The thermal model was validated against analytical solutions available for the 1D transient heat conduction equation. Equation (13) gives the surface temperature response of a single substrate subjected to a unit step change in gas temperature. The solution to a unit step change in gas temperature can be used to compute the response to a 421 K step change in gas temperature using the impulse response technique. The thermal model was run with a 421 K step change in gas temperature as the boundary condition for the squealer rim outer wall. The material property of the entire squealer cube was set to polyimide to behave as a

single substrate. Figure 21 compares the analytical solution with the response from the thermal model. The 3D model under-predicts the temperature rise by  $\sim 2\%$  because of three-dimensional diffusion of heat in the thermal model compared to one-dimensional diffusion in the analytical solution.

$$T_1(t) = 1 - \exp\left(\frac{-htc^2t}{(\rho C_p k)^2}\right) \operatorname{erfc}\left(\frac{htc\sqrt{t}}{\rho C_p k}\right) \quad (13)$$

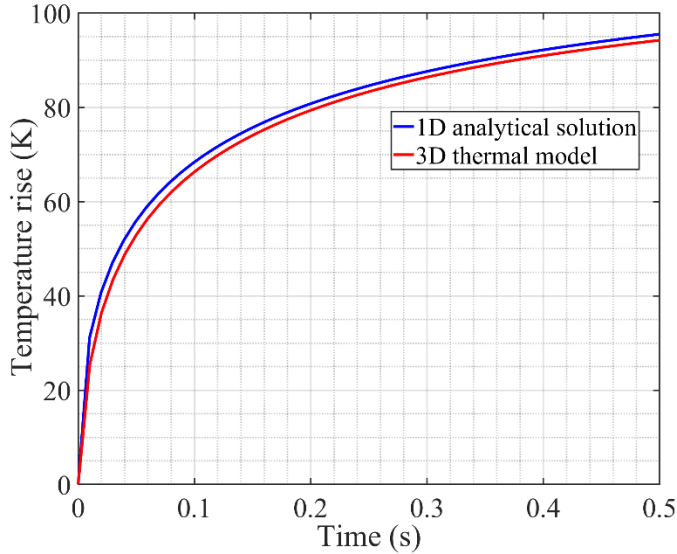


**FIGURE 21:** SURFACE TEMPERATURE RESPONSE OF A SEMI-INFINITE SINGLE-LAYER SUBSTRATE TO 421 K STEP CHANGE IN GAS TEMPERATURE

Equations (14) & (15) give the 1D transient heat conduction solution for a two-layer substrate subjected to a step change in heat flux [17]. The material property of the squealer cube was set to Aluminum and 155 microns thick polyimide (thickness used in the OTRF experiments for the rotor surface thin-film gauges) on the squealer rim outer wall. Figure 22 compares the analytical solution with the 3D thermal model response for both the surface temperature ( $T_1$ ) rise and polyimide-aluminium interface temperature ( $T_2$ ) rise. Similarly, the model under-predicts the surface temperature rise by  $\sim 2\%$  because of the three-dimensional diffusion. Given the good agreement between the 1D analytical solution and 3D thermal model over the short test window, the three-dimensional diffusion effects of heat can therefore be neglected. Usandizaga [14] also reported that lateral conduction is negligible if the test time  $t$  is sufficiently short such that  $at \ll l^2$  where  $l$  is the lateral length over which significant temperature variations could occur.

$$T_1(t) = \frac{2}{\sqrt{\rho_1 C_{p1} k_1}} \left[ \sqrt{\frac{t}{\pi}} + \sum_{n=1}^{\infty} \left\{ 2A^n \sqrt{\frac{t}{\pi}} \exp\left(\frac{-k_s^2}{4t}\right) - \frac{k_s}{2} \operatorname{erfc}\left(\frac{k_s}{2\sqrt{t}}\right) \right\} \right] \quad (14)$$

$$T_2(t) = \frac{2(1+A)}{\sqrt{\rho_1 C_{p1} k_1}} \left[ \sum_{n=0}^{\infty} A^n \left\{ \sqrt{\frac{t}{\pi}} \exp\left(\frac{-k_a^2}{4t}\right) - \frac{k_a}{2} \operatorname{erfc}\left(\frac{k_a}{2\sqrt{t}}\right) \right\} \right] \quad (15)$$

where

$$A = \frac{\sqrt{\rho_1 C_{p1} k_1} - \sqrt{\rho_2 C_{p2} k_2}}{\sqrt{\rho_1 C_{p1} k_1} + \sqrt{\rho_2 C_{p2} k_2}}, \quad k_s = 2n \sqrt{\rho_1 C_{p1} k_1} \left(\frac{a}{k_1}\right),$$

$$k_a = (2n+1) \sqrt{\rho_1 C_{p1} k_1} \left(\frac{a}{k_1}\right)$$

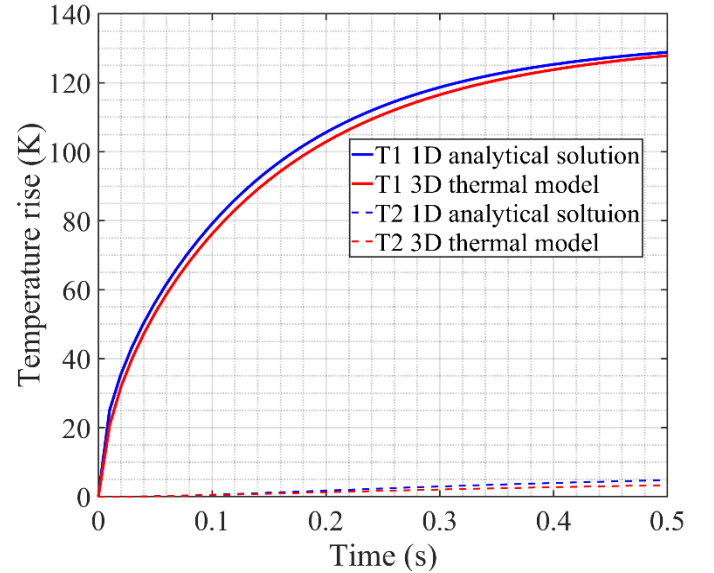


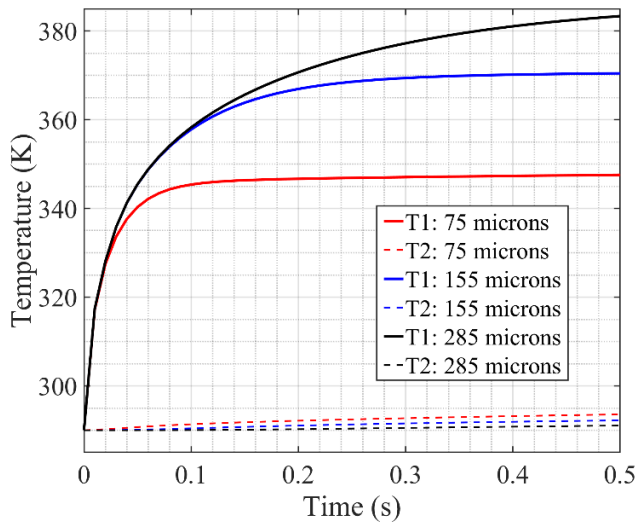
**FIGURE 22:** TEMPERATURE RESPONSE, AT THE SURFACE AND POLYIMIDE-ALUMINIUM INTERFACE, TO  $10^5 \text{ W/M}^2$  STEP CHANGE IN SURFACE HEAT FLUX FOR A SEMI-INFINITE TWO-LAYER SUBSTRATE

#### Application of thermal model:

The thermal model was used to study the effects of polyimide-adhesive package thickness on heat transfer data processing. A variety of package thickness were tested for the rotor surface polyimide sheet. Polyimide sheet thicker than 25 micron was found to form multiple creases when bending around the airfoil surface especially near the leading edge and tip region. The 3M adhesive in all its commercially available thicknesses i.e., 50, 130 and 260 microns, was found to be flexible to bend around the aerofoil, resulting in a total package thickness of 75, 155 and 285 microns possible for the rotor blade surface. Polyimide layer thickness in the thermal model was varied, and the surface temperature ( $T_1$ ) and interface temperature ( $T_2$ ) response were studied as shown in Figure 23. A thicker insulating substrate gives a higher temperature rise at a slower

rate compared to a thinner layer. The higher temperature rise improves the quality of the regression for Nusselt number and adiabatic wall temperature calculation. Compared to the 75 microns layer, the 285 microns and 155 microns layer gave 61% and 40% higher temperature rises respectively. The polyimide sheets were tested for survival in the OTRF at design speed, 285 microns layer was found to be bulky. As a result, a compromise was necessary leading to the use of 155 microns layer which survived during an OTRF spin test at 8500 rpm.

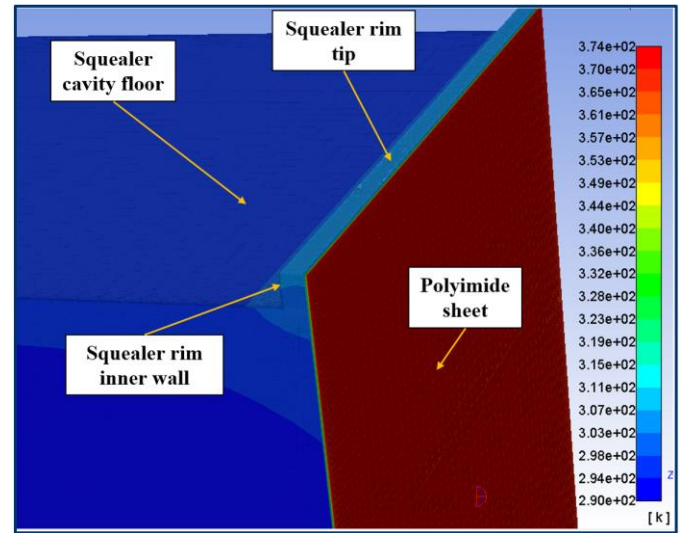
The thin-film gauge heat transfer analysis uses transient 1D heat conduction principles. The thermal model was used to understand the errors introduced in this 1D analysis by side conduction. The convective heat transfer boundary condition was imposed on the squealer cavity surface, rim tip and rim inner sidewall in addition to the polyimide squealer rim outer wall to model the side-conduction effects. Temperature was monitored on the polyimide surface ( $T_1$ ) and aluminium-polyimide interface ( $T_2$ ), both at 0.25 mm below the rim tip (this is the location of first row of thin-film gauges on the squealer rim of the rotor blade, as shown in Figure 12a, that will be subjected to a maximum side conduction).



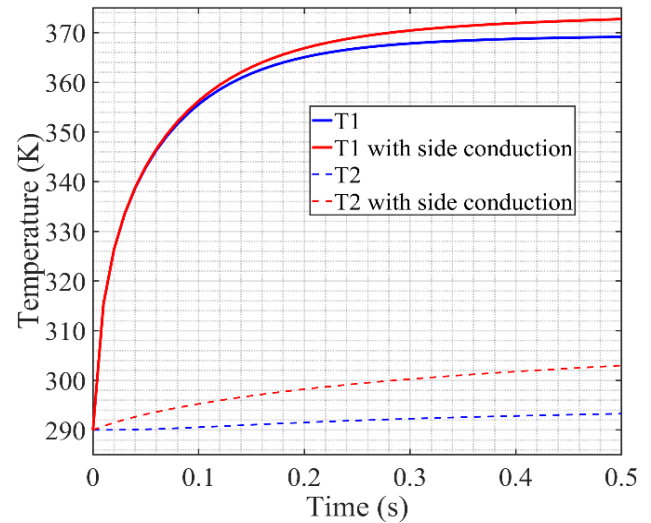
**FIGURE 23:** TEMPERATURE RESPONSE AT THE SURFACE AND POLYIMIDE-ALUMINIUM INTERFACE FOR A VARIETY OF POLYIMIDE-ADHESIVE LAYER THICKNESSES

Figure 24 illustrate the static temperature contour at various surfaces of the thermal model at the end of 0.5s. Polyimide, being a thermal insulator, achieves the highest temperature rise while aluminium, being a good conductor, dissipates the heat quicker and achieves a much lower temperature rise. Figure 25 compares the polyimide surface temperature ( $T_1$ ) and polyimide-aluminium interface temperature ( $T_2$ ) response from the thermal model with and without side-conduction. At the end of 0.5s, side-conduction (additional heat conducted through squealer cavity surface, squealer rim tip and squealer rim inner wall surfaces) had caused 4.5% additional rise in thin-film temperature and almost 300% additional rise in thermocouple temperature. Given the high thermal conductivity of aluminium compared to

polyimide, side-conduction has a much higher effect on the interface temperature than the polyimide surface.



**FIGURE 24:** STATIC TEMPERATURE CONTOUR 0.5 S AFTER THE THERMAL MODEL WAS SUBJECTED TO CONVECTIVE HEAT TRANSFER BOUNDARY CONDITION ON THE MARKED SURFACES



**FIGURE 25:** EFFECT OF SIDE-CONDUCTION ON TEMPERATURE RESPONSE AT THE POLYIMIDE SURFACE ( $T_1$ ) AND POLYIMIDE-ALUMINIUM INTERFACE ( $T_2$ )

The predicted temperature from the thermal model, both with and without side-conduction, was then processed using the impulse response technique described previously to compute heat flux. As shown in Figure 16, heat flux can be calculated in two ways: (1) Single sided gauge i.e. using just the polyimide surface temperature ( $T_1$ ) and an impulse response filter for a two layer substrate assuming a semi-infinite layer of aluminium, (2) Direct heat flux gauge i.e. using both polyimide surface temperature ( $T_1$ ) and polyimide-aluminium interface temperature ( $T_2$ ), and an impulse response filter for a two layer



substrate without assuming a semi-infinite aluminium substrate. Using the heat flux case without side-conduction as the nominal, a percentage error in heat flux was calculated based on Equation (16) for both single-sided and direct heat flux gauge configurations.

$$\% \text{ error in } q = \frac{q_{\text{side-conduction}} - q_{\text{nominal}}}{q_{\text{nominal}}} \times 100 \quad (16)$$

As shown in Figure 26, in both configurations, the absolute value of percentage error in heat flux increases with time as more heat is conducted through the sides. At the end of 0.5s, the direct heat flux gauge configuration experiences a - 6.4% error while the single-sided configuration experiences + 5.1% error. A 300% increase in interface temperature compared to just 4.5% increase in thin-film temperature due to side-conduction implies less driving temperature across the polyimide layer, and hence, heat flux calculations based on direct heat flux gauge configurations will have a higher and a negative error compared to a single-sided configuration. Assuming a uniform heat transfer coefficient across the polyimide surface, the thermal model presented in this paper helps understand the conduction of heat through multi-layer substrate in multiple directions. However, a squealer tip blade will have a spatial distribution of heat transfer coefficient that will be implemented in a future thermal model.

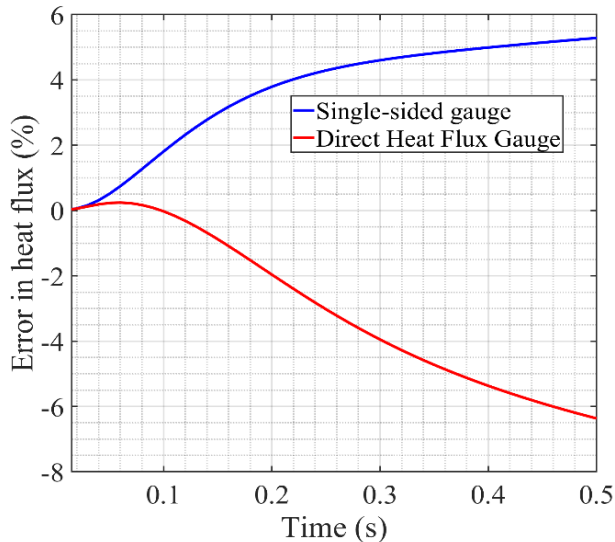


**FIGURE 26:** PERCENTAGE ERROR IN HEAT FLUX, DUE TO SIDE-CONDUCTION, PROCESSED USING TWO DIFFERENT METHODS

## 5 CONCLUSION

The single stage SILOET turbine, scaled from a modern civil engine, has been commissioned in the Oxford Turbine Research Facility. Calculation of mass flow rate for different flows in the OTRF has been presented. A non-dimensional heat loss factor (= 0.1035) was calculated to account for heat loss due to convection from the hot stream to the upstream rig components and, correctly calculate the mass-averaged stage

inlet total temperature. Turbine operating conditions have been established and most parameters were found to be within  $\pm 1\%$ , showing a good run to run consistency in the OTRF tests. An NGV inlet temperature profile survey was performed to measure the inlet RTDF temperature profile which is representative of a lean burn combustor exit.

Heat transfer measurement analysis using thin-film gauges has been presented covering the theory of operation, sensitivity, latest manufacturing and data-processing techniques. A method for calculating minimum substrate thickness required for 1D semi-infinite analysis to be valid has been presented. For the run time of the OTRF, this thickness value was found to be 600 microns. A parametric study for heat flux processed using the Impulse response method found heat flux to be most sensitive to the insulation layer thickness and its thermal product. The total probable uncertainty in heat flux was calculated as 3.3%. A thermal model, calibrated against analytical solutions, was developed to understand three-dimensional diffusion of heat and predict side-conduction effects for thin-film gauges instrumented in the near tip region of a squealer tip rotor blade. The model predicted + 5.1% and - 6.4% error due to side-conduction in heat flux when processed using a single-sided gauge and direct heat flux gauge configuration respectively.

The authors plan to publish a follow-up paper for this study covering the following aspects. A 3D CFD model calibrated against the experimental data. The heat transfer data from RTDF inlet condition was found to be more unsteady than Uniform condition tests, these will be quantified and presented. Novel methods of calculating derived heat transfer parameters such as Nusselt number and adiabatic wall temperature will also be discussed.

The commissioning of the turbine and heat transfer analysis presented in this paper provides a foundation for future experimental and computational studies on the SILOET turbine blade tip test campaign in the OTRF.

## ACKNOWLEDGEMENTS

The authors would like to acknowledge the financial support provided by Rolls-Royce plc for this project. The authors would also like to express gratitude to T. Godfrey for his expertise on instrumentation of thin-film gauges and S. Chana for his assistance in running the OTRF.

## REFERENCES

- [1] Arts, T. ed., 2004. *Turbine Blade Tip Design and Tip Clearance Treatment: January 19-23, 2003*. Von Karman Institute for Fluid Dynamics.
- [2] Sharma, O.P., and Stetson, G.M., "Impact of Combustor Generated Temperature Distortions on Performance, Durability and Structural Integrity of Turbines", VKI Lecture Series 1998-02, Feb.9-12, Brussels, Belgium, 1998
- [3] Hilditch, M.A., Fowler, A., Jones, T.V., Chana, K.S., Oldfield, M.L.G., Ainsworth, R.W., Hogg, S.I., Anderson, S.J., and Smith, G.C., 1994, "Installation of a turbine stage in the Pyestock Isentropic Light Piston Facility," ASME paper no. 94-GT-277.

- [4] Shahpar, S. and Caloni, S., 2013. Aerodynamic optimization of high-pressure turbines for lean-burn combustion system. *Journal of Engineering for Gas turbines and Power*, 135(5).
- [5] Beard, P.F., Povey, T. and Ireland, P.T., 2008. Mass flow rate measurement in a transonic turbine test facility with temperature distortion and swirl. *Flow Measurement and Instrumentation*, 19(5), pp.315-324.
- [6] Adams, M.G., Povey, T., Hall, B.F., Cardwell, D.N., Chana, K.S. and Beard, P.F., 2020. Commissioning of a combined hot-streak and swirl profile generator in a transonic turbine test facility. *Journal of Engineering for Gas Turbines and Power*, 142(3).
- [7] Chana, K.S., 1992. Heat transfer and aerodynamics of a high rim speed turbine nozzle guide vane with profiled end walls (Vol. 78965, p. V004T09A023). American Society of Mechanical Engineers.
- [8] Hall, B.F., Chana, K.S. and Povey, T., 2014. Design of a nonreacting combustor simulator with swirl and temperature distortion with experimental validation. *Journal of engineering for gas turbines and power*, 136(8).
- [9] Beard, P.F. (2010), "On transient turbine efficiency measurements with engine representative inlet flows," DPhil thesis, University of Oxford.
- [10] Chana, K.S. and Jones, T.V., 2003. An investigation on turbine tip and shroud heat transfer. *J. Turbomach.*, 125(3), pp.513-520.
- [11] Schultz, D.L. and Jones, T.V., 1973. Heat-transfer measurements in short-duration hypersonic facilities (No. AGARD-AG-165). ADVISORY GROUP FOR AEROSPACE RESEARCH AND DEVELOPMENT PARIS (FRANCE).
- [12] Collins, M., Chana, K. and Povey, T., 2015. New technique for the fabrication of miniature thin film heat flux gauges. *Measurement science and technology*, 26(2), p.025303.
- [13] Piccini, E., Guo, S.M. and Jones, T.V., 2000. The development of a new direct-heat-flux gauge for heat-transfer facilities. *Measurement Science and Technology*, 11(4), p.342.
- [14] Usandizaga, I., Beard, P., Chana, K. and Povey, T., 2020. Heated thin film gauge arrangements to reduce uncertainty in transient heat transfer measurements. *Measurement Science and Technology*, 32(1), p.015906.
- [15] Neugebauer, C.A. and Webb, M.B., 1962. Electrical conduction mechanism in ultrathin, evaporated metal films. *Journal of Applied Physics*, 33(1), pp.74-82.
- [16] Doorly, J.E. and Oldfield, M.L.G., 1987. The theory of advanced multi-layer thin film heat transfer gauges. *International journal of heat and mass transfer*, 30(6), pp.1159-1168.
- [17] Oldfield, M.L.G., 2008. Impulse response processing of transient heat transfer gauge signals. *Journal of turbomachinery*, 130(2).
- [18] Kline, S.J., 1953. Describing uncertainty in single sample experiments. *Mech. Engineering*, 75, pp.3-8.
- [19] Moffat, R.J., 1982. Contributions to the theory of single-sample uncertainty analysis.